remote sensing

MDPI

Article

A Two-Stage Decoupling Framework for Blind Hyperspectral Unmixing: Separately Refining Endmembers and Abundances

Hengnuo Liu, Yulin Zhang, Yanyan Li *, Yongli Wang and Xiuchuan Chen

College of Mathematics and Systems Science, Shandong University of Science and Technology, Qingdao 266590, China; 202311081009@sdust.edu.cn (H.L.); zhangyulin@sdust.edu.cn (Y.Z.); wangyongli@sdkd.net.cn (Y.W.); 202582150017@sdust.edu.cn (X.C.)

* Correspondence: liyanyan@sdust.edu.cn

Highlights

What are the main findings?

- The relationship between endmembers and abundances in NMF-based multi-variable joint optimization problems (NMF-based JOPs) is intrinsically coupled under noise, making it difficult to simultaneously improve their estimation accuracy.
- The hard abundance sum-to-one constraint (ASC) is inconsistent with realistic noisy conditions, preventing accurate estimation of endmembers and abundances simultaneously.

What are the implications of the main findings?

- A two-stage decoupling framework is proposed to address the intrinsic coupling, enabling separate refinement of endmembers and abundances.
- The proposed L_1-SoftASC formulation allows accurate abundance estimation under noise by relaxing the ASC while preserving sparsity.

Abstract

Hyperspectral unmixing (HU) aims to estimate endmembers and their corresponding abundances, a task commonly referred to as blind hyperspectral unmixing (BLU). Nonnegative matrix factorization (NMF) provides a unified framework for their joint estimation. It is widely assumed that more accurate endmember estimation leads to improved abundance estimation, enabling simultaneous optimization of both variables. However, this paper shows that, in practical noisy scenarios, the relationship between endmembers and abundances in NMF-based multi-variable joint optimization problems (NMF-based JOPs) is inherently coupled and significantly more complex, making it difficult to improve both estimation accuracies simultaneously. Furthermore, we demonstrate that the hard abundance sum-to-one constraint (ASC), commonly imposed in NMF-based JOPs, is inconsistent with realistic noisy conditions. To address these limitations, we propose a novel two-stage framework for BLU that decouples the refinement of endmembers and abundances. In the first stage, a strongly convex minimum-volume simplex model is employed to ensure robust and stable endmember extraction. In the second stage, we introduce a novel formulation, L_1_SoftASC, which promotes abundance sparsity and physical interpretability while improving convexity and robustness in abundance estimation. Experimental results on both synthetic and real benchmark datasets demonstrate that the proposed two-stage approach consistently outperforms existing single-stage NMF-based JOP methods in terms of both endmember and abundance estimation accuracy, while providing BLU with greater flexibility in handling ASC.

Check for updates

Academic Editor: Mohammadmehdi Saberioon

Received: 18 May 2026
Revised: 11 June 2026
Accepted: 15 June 2026
Published: 25 June 2026

Copyright: © 2026 by the authors. Licensee MDPI, Basel, Switzerland. This article is an open access article distributed under the terms and conditions of the Creative Commons Attribution (CC BY) license.

Keywords: blind hyperspectral unmixing (BHU); minimum-volume simplex; L_1 regularization; two-stage methods (TSMs); single-stage methods (SSMs); soft abundance sum-to-one constraint (SoftASC); nonnegative matrix factorization (NMF)

1. Introduction

Hyperspectral images (HSIs) have been widely used in various applications, such as anomaly detection, land-cover classification, environmental monitoring, and mineral mapping, owing to their rich spectral information. However, the observed spectral signals are often mixed due to the limited spatial resolution of imaging sensors. Linear hyperspectral unmixing (LHU) is a fundamental and widely adopted technique for decomposing each pixel in an HSI into a set of endmembers and their corresponding abundance fractions. Due to the high dimensionality of HSIs and the statistical dependencies among spectral vectors, LHU has remained a long-standing research topic. In most practical scenarios, both the endmembers and their corresponding abundances are unknown. This setting is referred to as blind hyperspectral unmixing (BLU). Representative approaches for BLU include statistical methods [1–3] and deep learning-based methods [4–6]. Among these, one of the most widely adopted frameworks is nonnegative matrix factorization (NMF) [2,4,7–12], which formulates BLU as a joint optimization problem over two matrix variables: the endmember matrix $\mathbf{M}$ and the abundance matrix $\mathbf{S}$. NMF-based methods are computationally tractable and can be efficiently implemented using modern optimization algorithms. Moreover, they enable the simultaneous estimation of both endmembers and abundances within a unified framework.

To improve performance, extensive efforts have been devoted to enhancing NMF-based models from an optimization perspective, primarily by incorporating various regularization terms into the objective function. Typical examples include:

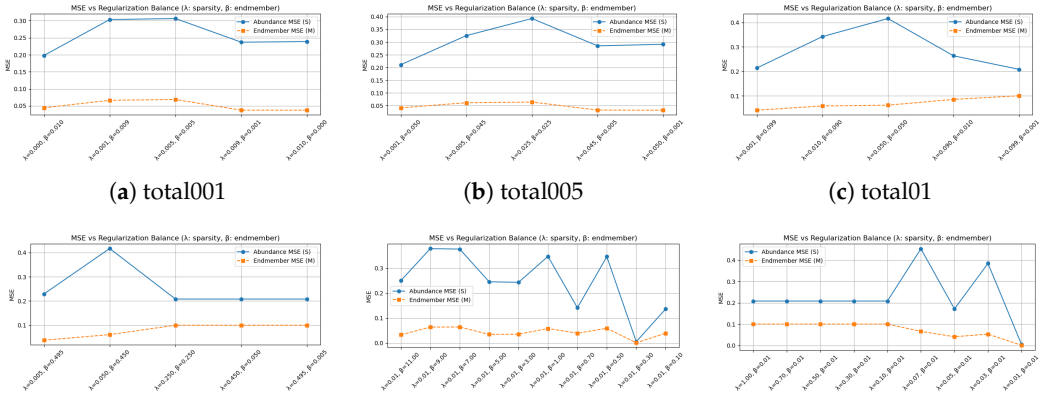
- Volume regularization on the endmember matrix (e.g., NMF-QMV [7]);
- L_1-norm regularization on the abundance matrix to promote sparsity [8];
- Total variation (TV) regularization to encourage spatial smoothness in abundance maps [4,9].

Each regularization term is typically associated with a hyperparameter to balance data fidelity and prior constraints. Consequently, advanced NMF-based models often involve complex objective functions with multiple variables and two or more hyperparameters (see model (1) in Section 2.2). Such increased model complexity inevitably introduces trade-offs in estimation accuracy.

Moreover, there are two limitations in NMF-based multi-variable joint optimization problems (NMF-based JOPs), which motivate our work. The first limitation concerns the commonly held assumption that more accurate endmember estimation necessarily leads to more accurate abundance estimation. In contrast, we demonstrate in Section 3.1 that this assumption does not always hold in real-world scenarios with noise. Specifically, the relationship between endmembers and abundances is inherently complex, exhibiting multiple possible behaviors (see Figure 1), and there is no general principle to guarantee simultaneous high accuracy for both variables. Variations in endmember estimates inevitably affect the corresponding abundances, indicating a strong coupling between the two. As shown in Section 3.1, this coupling phenomenon is pervasive in NMF-based JOPs, yet it has not been explicitly addressed in the existing literature. Motivated by the challenges arising from such coupled uncertainties, we propose a two-stage framework in which the two variables are treated separately. In the first stage, we focus solely on endmember estimation.

Building upon our previous work, highly accurate endmembers can be obtained using a strongly convex minimum-volume simplex formulation.

The second limitation is that, even with accurate endmembers, NMF-based JOPs with a hard ASC fail to achieve highly accurate abundance estimation in the presence of noise (see Section 3.1). In other words, existing approaches are unable to attain high accuracy for both endmembers and abundances simultaneously under realistic conditions, a limitation that has not been previously recognized. In LHU literature, ASC has been dealt with in two different ways: hard ASC and soft ASC. Hard ASC refers to strictly satisfying ASC, i.e., ASC. In this setting, Fully Constrained Least Squares Unmixing (FCLSU) [13] and the Projection onto Simplex (Proj) method [14] are two representative exact approaches. Soft ASC refers to relaxation of ASC in certain ways. For example, sparse regression-based unmixing [15] can be regarded as a relaxed formulation, which typically employs the L_1 norm to promote sparsity in the abundance estimates. However, this approach is overly relaxed in that it neglects the ASC. The underlying reason is that enforcing ASC renders the L_1 norm constant, thereby eliminating its ability to regulate sparsity.



(**a**) total001 (**b**) total005 (**c**) total01

(**d**) total05 (**e**) fix_lam01 (**f**) fix_beta01

Figure 1. Mean squared error (MSE) of estimated endmembers (**M**) and abundances (**S**) under different regularization settings. (**a**–**d**): Fixed total regularization strength ($\lambda + \beta = 0.001, 0.005, 0.01, 0.05$) with varying ratio between λ and β. (**e**): Fixed $\lambda = 0.01$ with decreasing β. (**f**): Fixed $\beta = 0.01$ with decreasing λ.

Between these two extremes of exact ASC and omitting ASC, there exist moderately relaxed approaches that partially relax the ASC. These methods have demonstrated that, in certain cases, the strict enforcement of ASC may be overly restrictive, and that relaxing this constraint can lead to improved abundance estimation accuracy. For instance, refs. [16,17] allow small deviations from the strict ASC, improving performance in terrain-influenced scenarios. The RMVSA method [18] introduces a probabilistic relaxation of the abundance nonnegativity constraint (ANC) using chance constraints. Similarly, MAP-based methods [19] model ASC and ANC as Gaussian priors, enabling soft enforcement within a maximum a posteriori framework. Specifically, they use a Gaussian distribution centered at the simplex centroid with a covariance matrix representing permissible deviations. However, the relaxation related papers have not addressed in detail the reason why the exact methods are superior to the relaxed ones.

To address this issue, we introduce a SoftASC strategy in the second stage, where the endmembers are fixed based on the first-stage estimation. The proposed SoftASC relaxes the ASC in a principled manner by penalizing deviations from the sum-to-one condition, rather than enforcing it strictly. Compared with existing SoftASC formulation in the literature, the proposed formulation is deterministic and retains clear interpretability. It can explicitly quantify the degree of violation of the sum-to-one constraint. Moreover, it is a

strongly convex and differentiable function, which is beneficial for computational efficiency. Beyond its practical advantages, this formulation also provides a new perspective on how ASC can be modeled and utilized in hyperspectral unmixing frameworks.

The contributions of this work are threefold:

(1) Identification of the coupling phenomenon

This paper presents an explicit identification and analysis of the coupling phenomenon in NMF-based JOPs, which has received limited attention in existing studies. We demonstrate that this intrinsic coupling effect fundamentally limits the simultaneous improvement of endmember and abundance estimation accuracy. This finding provides new theoretical insight into the limitations of existing joint optimization frameworks and offers a clear motivation for developing decoupled optimization strategies.

(2) A novel two-stage framework

We show that NMF-based JOPs are inherently unable to overcome the coupling effect and, consequently, cannot achieve high accuracy for both endmembers and abundances simultaneously. To address this issue, we propose a novel two-stage framework that explicitly decouples endmember extraction and abundance estimation within the NMF context. In the first stage, the model focuses exclusively on endmember estimation, retaining only endmember-related regularization terms. In the second stage, abundance inversion is performed with the ASC relaxed via a penalty on deviations from the ASC. As demonstrated by Case 3) in Section 3.1, both the two-stage design and the SoftASC formulation are essential for achieving high-accuracy estimation of both endmembers and abundances.

(3) L_1_SoftASC model for abundance estimation under noise

We propose a novel L_1_SoftASC formulation for abundance estimation in noisy scenarios. Compared with the other SoftASC-related methods mentioned above, the proposed quadratic soft-constraint formulation can be naturally incorporated together with the L1-norm regularization. By contrast, other probabilistic constraint formulations are less straightforward to combine with L1-norm based modeling. This design simultaneously promotes sparsity and physical interpretability of abundances, while improving convexity and robustness of the optimization problem. It reconciles the long-standing conflict between sparsity promotion and strict enforcement of the ASC. Beyond its practical advantages, this formulation also provides a new perspective on how ASC can be modeled and utilized in hyperspectral unmixing, revealing that ASC can be relaxed in a principled manner to achieve both sparsity and robustness under realistic conditions.

2. Materials

2.1. Linear Hyperspectral Unmixing Models

Given the observed hyperspectral matrix $\mathbf{Y}_{l\times n}$, LHU aims to find the endmember matrix $\mathbf{M}_{l\times p}$ and the abundance matrix $\mathbf{S}_{p\times n}$, which satisfies the following conditions:

$$\begin{aligned}\mathbf{Y}_{l\times n} &= \mathbf{M}_{l\times p}\mathbf{S}_{p\times n} + \mathbf{N},\\ s.t.\ \mathbf{S}_{p\times n} &\geq \mathbf{0}_{p\times n},\ \mathbf{1}_p^\top \mathbf{S}_{p\times n} = \mathbf{1}_n^\top\end{aligned}$$

where $\mathbf{N} \in \mathbb{R}^{l\times n}$ represents perturbations, such as noise or model deviations, and p, l, and n denote the number of endmembers, spectral bands, and pixels, respectively. The constraints are referred to as the abundance nonnegativity constraint (ANC) and the abundance sum-to-one constraint (ASC).

2.2. Nonnegative Matrix Factorization-Based Muti-Variable Joint Optimization Problems (NMF-Based JOPs)

Nonnegative matrix factorization-based regularized models are typically formulated as [20–22]:

$$\begin{aligned} \min_{\mathbf{M},\mathbf{S}} \quad & \frac{1}{2}\|\mathbf{Y}_{l\times n} - \mathbf{M}_{l\times p}\mathbf{S}_{p\times n}\|_F^2 + \lambda_V R(\mathbf{M}_{l\times p}) \\ & +\lambda_1\|\mathbf{S}_{p\times n}\|_1 + \lambda_{TV}\|\mathbf{S}_{p\times n}\|_{TV}, \\ s.t. \quad & \mathbf{S}_{p\times n} \geq \mathbf{0}_{p\times n},\ \mathbf{1}_p^\top \mathbf{S}_{p\times n} = \mathbf{1}_n^\top, \end{aligned} \tag{1}$$

where $\frac{1}{2}\|\mathbf{Y}_{l\times n} - \mathbf{M}_{l\times p}\mathbf{S}_{p\times n}\|_F^2$ represents the data fidelity, $R(\cdot)$ denotes some regularization function, the L_1 norm of $\mathbf{S}$ is used to improve sparsity and the TV term on $\mathbf{S}$ can enhance spatial smoothness.

A commonly used solver is the alternative direction multiplier method (ADMM), which decomposes the above model into four or five subproblems and minimizes them in an alternating manner. The algorithm obtains endmembers and abundances simultaneously. To distinguish them from the proposed two-stage framework, we refer to JOPs as NMF-based single-stage methods (SSMs).

3. Methods

3.1. A Unified Two-Stage Decoupling Unmixing Framework

This study is motivated by two previously overlooked limitations in NMF-based JOPs, which hinder their ability to achieve highly accurate estimation of both endmembers and abundances simultaneously.

Limitation 1. *More accurate endmembers do not necessarily lead to more accurate abundances in NMF-based JOPs.*

We illustrate this phenomenon through the following three cases.

(1) Ideal Case without Noise

If the hyperspectral image strictly follows the noise-free linear mixing model

$$\mathbf{Y} = \mathbf{M}_{\text{true}}\mathbf{S}_{\text{true}}, \tag{2}$$

then improving the estimation accuracy of $\mathbf{M}$ directly leads to improved accuracy of the estimated abundances $\mathbf{S}$. In this well-conditioned setting, the interaction between the two variables is consistent and predictable, allowing both endmembers and abundances to be accurately estimated simultaneously.

(2) Noisy Case with Inaccurate Endmembers

Consider a more realistic scenario

$$\mathbf{Y} = \mathbf{M}_{\text{true}}\mathbf{S}_{\text{true}} + \mathbf{N}, \tag{3}$$

where $\mathbf{N}$ denotes noise or model mismatch. In this case, the relationship between $\mathbf{M}$ and $\mathbf{S}$ becomes significantly more complex.

To illustrate this behavior, we consider the following joint optimization problem:

$$\begin{aligned} \min_{\mathbf{M},\mathbf{S}} \quad & \frac{1}{2}\left\|\mathbf{Y}_{l\times n} - \mathbf{M}_{l\times p}\mathbf{S}_{p\times n}\right\|_F^2 + \lambda\left\|\mathbf{S}_{p\times n}\right\|_1 \\ & +\beta\left\|\mathbf{M}_{l\times p}\right\|_F^2 \\ s.t. \quad & \mathbf{S}_{p\times n} \geq \mathbf{0}_{p\times n},\ \mathbf{1}_p^\top \mathbf{S}_{p\times n} = \mathbf{1}_n^\top. \end{aligned} \tag{4}$$

A synthetic example is constructed with randomly generated data ($p = 3$, $l = 10$, $n = 200$). We consider three settings:

(i) Fixed total regularization strength ($\lambda + \beta = 0.001, 0.005, 0.01, 0.05$) with varying ratio;
(ii) Fixed $\lambda = 0.01$ with decreasing β;
(iii) Fixed $\beta = 0.01$ with decreasing λ.

For each setting, alternating minimization (AM) is applied as follows:

$$\mathbf{E}^1 \to \mathbf{S}^1 \to \cdots \to \mathbf{E}^k \to \mathbf{S}^k \cdots \to \mathbf{E}^* \to \mathbf{S}^*$$

The MSE of both **M** and **S** are used for evaluation. Across all configurations in Figure 1a–f, both abundance and endmember estimation errors exhibit non-monotonic and inconsistent trends. In particular, reducing one variable error does not necessarily reduce the other. In single-variable optimization, increasing the regularization weight λ (for abundances) typically improves certain properties of the solution (e.g., sparsity or smoothness). In contrast, in joint optimization, because **M** and **S** jointly contribute to the reconstruction, constraining one variable changes the role of the other in explaining the data, leading to interdependent estimation errors. In other words, this behavior can be explained by the intrinsic coupling between **M** and **S** in the reconstruction term. Therefore, the optimization problem is intrinsically coupled, and it is difficult to simultaneously achieve high accuracy for both endmembers and abundances within a single joint optimization framework.

Assume that the true data follow (3) and that the exact endmembers $\mathbf{M}_{\text{true}}$ are available.

Under the hard ASC constraint, the abundance estimation is given by

$$\mathbf{Y} = \mathbf{M}_{\text{true}}\mathbf{S}_{\text{esti}}. \tag{5}$$

Comparing (3) and (5), it is evident that $\mathbf{S}_{\text{esti}}$ deviates from $\mathbf{S}_{\text{true}}$, due to the presence of noise. This indicates that even with perfectly accurate endmembers, the estimated abundances remain biased when the hard ASC is enforced. Otherwise, it indicates that $\mathbf{Y} = \mathbf{M}_{\text{true}}\mathbf{S}_{\text{true}}$, which is inconsistent with (3).

Limitation 2. *NMF-based JOPs with hard ASC cannot achieve high accuracy for both endmembers and abundances simultaneously.*

If both **M** and **S** were estimated with high accuracy under the hard ASC, such that (5) holds exactly, it would contradict the realistic noisy model in (3). Therefore, enforcing a strict ASC inherently limits the achievable abundance accuracy in the presence of noise.

From the above two limitations, it can be observed that the main challenge in NMF-based JOPs is not merely parameter tuning, but rather the intrinsic coupling. To address this issue, we propose a unified two-stage decoupling framework (Figure 2), which aims to break this coupling and optimize the two variables separately.

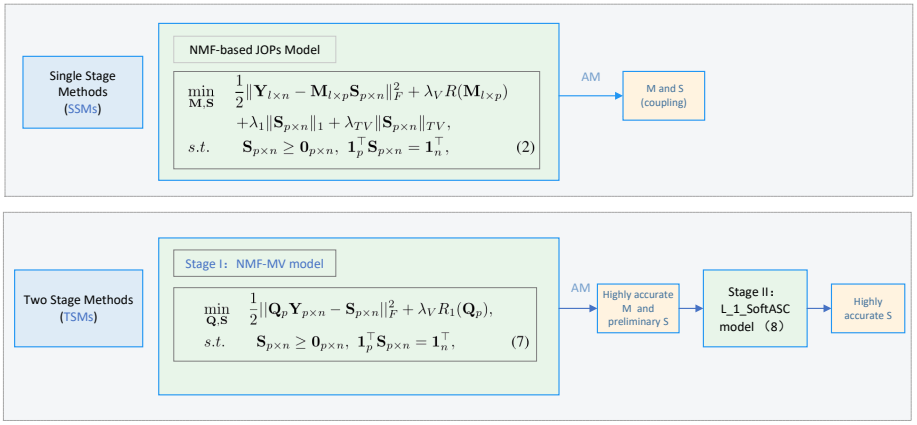


Figure 2. Comparison of single-stage methods (SSMs) and the proposed two-stage methods (TSMs).

In the first stage, we focus on endmember extraction and retain only the regularization on **M** (NMF_MV model). The abundance matrix **S** is obtained as an exact mapping of the endmembers using the Proj method. This formulation leads to more stable and accurate endmember estimation.

In the second stage, the estimated endmembers are fixed, thereby eliminating the coupling effect. Motivated by the analysis in Case 3, we relax the ASC by introducing a soft penalty that allows deviations from the sum-to-one constraint, improving adaptability to noise. Meanwhile, the L_1 regularization is preserved to promote sparsity. This leads to the proposed L_1_SoftASC model, which enhances abundance estimation while maintaining favorable convexity properties.

By decoupling the optimization process, the proposed framework effectively avoids the trade-offs inherent in joint optimization and enables more accurate estimation of both endmembers and abundances.

3.2. A Novel Two-Stage Unmixing Method Based on Strongly Convex Minimum Volume Simplex and L_1_SoftASC

Based on the proposed two-stage framework, we develop a novel hyperspectral unmixing method. In the first stage, a strongly convex minimum-volume simplex model is employed, which ensures stable optimization performance and eliminates the need for VCA-based initialization. The second stage introduces a novel formulation that combines L_1 sparsity regularization with a soft abundance sum-to-one constraint (SoftASC). This formulation is shown to outperform conventional approaches that either rely solely on L_1 regularization while neglecting the ASC, or enforce the ASC as a hard constraint.

3.2.1. Stage I: Endmember Extraction via a Strongly Convex Minimum Volume Simplex Model

To overcome the limitations caused by the non-convexity issue in SISAL [23], our previous work [24] proposed the following strongly convex NMF-MV model:

$$\begin{aligned} \min_{\mathbf{Q},\mathbf{S}} \quad & \frac{1}{2}||\mathbf{Q}_p\mathbf{Y}_{p\times n} - \mathbf{S}_{p\times n}||_F^2 + \lambda_V R_1(\mathbf{Q}_p), \\ s.t. \quad & \mathbf{S}_{p\times n} \geq \mathbf{0}_{p\times n},\ \mathbf{1}_p^\top \mathbf{S}_{p\times n} = \mathbf{1}_n^\top, \end{aligned} \tag{6}$$

Since the observed hyperspectral matrix $\mathbf{Y}_{l\times n}$ typically exhibits significant spectral redundancy due to the high correlation among spectral bands, principal component analysis (PCA) is first applied to reduce the data dimensionality by projecting it onto a lower-dimensional subspace spanned by the p leading principal components. In this reduced

subspace, the projected endmember matrix $\mathbf{M}_p$ has full column rank and is therefore invertible. For convenience, we denote its inverse by $\mathbf{Q}_p$, i.e., $\mathbf{Q}_p := \mathbf{M}_p^{-1}$. The parameter λ_V is a trade-off coefficient balancing data fidelity and the volume regularization term. A small positive constant ε is introduced to prevent numerical instability. The volume regularization term is defined as

$$R_1(\mathbf{Q}_p) := -\frac{1}{2}\log\Big\{\det\Big[(\mathbf{Q}_p + \varepsilon\mathbf{I}_p)^\top(\mathbf{Q}_p + \varepsilon\mathbf{I}_p)\Big]\Big\},$$

By penalizing ill-conditioned matrices, $R_1(\mathbf{Q})$ discourages degenerate solutions. It should be noted that in minimum-volume simplex methods combined with PCA-based dimensionality reduction, the optimization variable is typically not (M) itself, but rather the inverse matrix of the endmembers in the reduced subspace. Therefore, nonnegativity is usually not explicitly enforced during this stage [23,25].

The model is optimized using an AM strategy. For the $\mathbf{Q}_p$-subproblem, where $\mathbf{S}$ is fixed, we adopt the adaptive moment method (Adam), a first-order optimizer that does not require computing Hessians. Since the objective function in this subproblem is strongly convex, smooth, and Lipschitz continuous [26], Adam achieves linear convergence.

Notably, the strong convexity of $R_1(\mathbf{Q}_p)$ ensures stable optimization and removes the need for VCA-based initialization. For further details on the choice of specific initial points and the influence of initialization on different methods, interested readers are referred to [24]. To the best of our knowledge, most existing MV-based methods depend heavily on VCA initialization.

For the $\mathbf{S}$-subproblem, where $\mathbf{Q}$ is fixed, the task reduces to projecting onto a probability simplex. As shown in [14], this projection has a unique solution that can be computed efficiently. We denote this operation as $\mathbf{S} = \mathrm{proj}(\mathbf{Q})$.

The full alternating minimization algorithm used in Stage I is summarized in Algorithm 1.

Algorithm 1 First Stage: AM for the CMV Model

Input: Initial variable Q^0; parameters $\alpha = 10^{-3}$, $\rho_1 = 0.9$, $\rho_2 = 0.999$, $\delta = 10^{-8}$; initial moments $m_0 = \mathbf{0}$, $\nu_0 = \mathbf{0}$; stopping tolerance $\tau = 10^{-6}$; penalty parameter $\mu = 0.1$; regularization parameter $\lambda = 4$; $\varepsilon = 5$, $k \leftarrow 1$, $g_0 \leftarrow \nabla\varphi(Q^0)$
while $\|g_{k-1}\| \geq \tau$ **do**
  Update S**:**
  Solve the S-subproblem: $S^{k-1} \leftarrow \mathrm{Proj}(Q^{k-1})$ [14]
  Update Q**:**
  $g_{k-1} \leftarrow \nabla\varphi(Q^{k-1})$
  $m_k \leftarrow \rho_1 m_{k-1} + (1-\rho_1)g_{k-1}$
  $\nu_k \leftarrow \rho_2\nu_{k-1} + (1-\rho_2)(g_{k-1} \odot g_{k-1})$
  $\hat{m}_k \leftarrow \frac{m_k}{1-\rho_1^k}$
  $\hat{\nu}_k \leftarrow \frac{\nu_k}{1-\rho_2^k}$
  $Q^k \leftarrow Q^{k-1} - \alpha\frac{\hat{m}_k}{\sqrt{\hat{\nu}_k+\delta I}}$
  $k \leftarrow k+1$
  $\lambda \leftarrow \mu\lambda$
  $\varepsilon \leftarrow 0.9\varepsilon$
end while
Output: Optimized variables Q^*

The symbol $\odot$ denotes element-wise multiplication. The gradient of the objective function in the (k−1)th iteration is

$$\begin{aligned} g_{k-1} &= \nabla\left(\tfrac{1}{2}\|\mathbf{QY}-\mathbf{S}\|_F^2 - \lambda_V R_1(\mathbf{Q})\right) \\ &= (\mathbf{QY}-\mathbf{S})\mathbf{Y}^\top - \lambda_V(\mathbf{Q}+\varepsilon\mathbf{I})^{-\top} \end{aligned}$$

Denoting the optimal solution as $\mathbf{Q}_p$, the endmember matrix is obtained as $\mathbf{M}_p = \mathbf{Q}_p^{-1}$.

We have demonstrated that the accuracy of extracted endmembers, evaluated using metrics such as SAD and NMSE, often surpasses that of state-of-the-art methods. However, the abundance estimates tend to be less competitive. In fact, the abundance is solved by the exact method Proj and with hard ASC.

Based on the analysis in Section 3.1, this paper points out that due to the coupling between two variables in SSMs, higher accurate endmembers do not imply higher accurate abundances. In addition, combined with Case (3) in Section 3.1, it is again validated that hard ASC may cause inaccurate abundances in noisy situations.

3.2.2. Stage II: L_1_SoftASC Model for Abundance Estimation

With the optimal $\mathbf{Q}_p$ obtained in the first stage, abundances can be estimated by solving the following problem using traditional projection-based or FCLS-type methods [13,26,27]:

$$\begin{aligned} \min_{\mathbf{S}} \quad & \frac{1}{2}||\mathbf{Q}_p\mathbf{Y}_{p\times n} - \mathbf{S}_{p\times n}||_F^2 \\ s.t. \quad & \mathbf{S}_{p\times n} \geq \mathbf{0}_{p\times n},\ \mathbf{1}_p^\top \mathbf{S}_{p\times n} = \mathbf{1}_n^\top, \end{aligned} \tag{7}$$

Model (7) represents an ideal scenario where endmembers are accurate and the ASC strictly holds. However, in real-world conditions involving sensor noise, reflectance interactions, or spectral variability, measured endmembers often deviate from their ideal spectra, making the strict ASC infeasible. Rigidly enforcing the ASC under such conditions may lead to biased or unstable abundance estimates.

In recent years, L_1-norm regularization on abundances, $||\mathbf{S}_{p\times n}||_1$, has been widely adopted to promote sparsity and improve abundance estimation quality [8,23]. However, in conventional HU models that employ L_1 regularization, the ASC is often neglected, because under a hard ASC, the L_1 norm becomes constant and thus loses its effectiveness as a sparsity-promoting regularizer. This long-standing conflict between enforcing sparsity and maintaining physical interpretability has not been properly addressed in the literature.

Based on the above analysis, we propose a new deterministic and convex formulation, denoted as L_1_SoftASC:

$$\begin{aligned} \min_{\mathbf{S}} \quad & \frac{1}{2}||\mathbf{Q}_p\mathbf{Y}_{p\times n} - \mathbf{S}_{p\times n}||_F^2 + \mu||\mathbf{S}_{p\times n}||_1 \\ & +\tau\sum_{j=1}^{n}\left(\mathbf{1}_p^\top \mathbf{s}_j - 1\right)^2 \\ s.t. \quad & \mathbf{S}_{p\times n} \geq \mathbf{0}_{p\times n}, \end{aligned} \tag{8}$$

where μ is the sparse regularization parameter, τ controls the degree of relaxation of the ASC, and $\mathbf{s}_j$ denotes the j^{th} column of $\mathbf{S}_{p\times n}$. The quadratic penalty $\tau\sum_{j=1}^{n}(\mathbf{1}_p^\top \mathbf{s}_j - 1)^2$ softly enforces the ASC while allowing limited deviations to enhance robustness under noisy or variable conditions.

The proposed L_1_SoftASC formulation (8) has the following advantages:

(1) Robustness to real-world conditions.

The SoftASC term introduces a quadratic penalty on deviations from the ASC, allowing limited flexibility while maintaining the physical interpretability of abundances. This enhances robustness under noise, endmember variability, or illumination changes.

(2) Simultaneous preservation of sparsity and physical interpretability.

It reveals that ASC can be relaxed in a principled way without losing its physical meaning, thus bridging the gap between sparse and physically constrained unmixing frameworks.

(3) Deterministic and convex optimization.

Unlike probabilistic relaxations such as RMVSA [18] or MAP-based Gaussian priors [19], the proposed SoftASC offers a deterministic and convex formulation that is straightforward to integrate into standard optimization frameworks. In addition, the convex property helps the optimization avoid local minima while maintaining computational efficiency and interpretability.

Theorem 1. *The function $f_1(\mathbf{S})$ is strongly convex in $\mathbb{R}^{p\times n}$.*

Proof. The gradient of f_1 with respect to $\mathbf{S}$ is:

$$\nabla f_1 = \mathbf{S} - \mathbf{QY} + 2\tau\Big[\Big(\mathbf{1}_p^\top \mathbf{s}_1 - 1\Big)\mathbf{1}_p, \ldots, \Big(\mathbf{1}_p^\top \mathbf{s}_n - 1\Big)\mathbf{1}_p\Big].$$

The Hessian of f_1 is:

$$\nabla^2 f_1 = \mathbf{I}_{pn} + 2\tau \cdot \mathrm{diag}\left(\underbrace{\mathbf{1}_p\mathbf{1}_p^\top, \ldots, \mathbf{1}_p\mathbf{1}_p^\top}_{n \text{ blocks}}\right),$$

where each block $\mathbf{1}_p\mathbf{1}_p^\top \in \mathbb{R}^{p\times p}$ is a rank-one positive semidefinite matrix. The operator $\mathrm{diag}(\cdot)$ forms a block diagonal matrix. Since $\mathbf{I}_{pn}$ is positive definite and the second term is positive semidefinite, the Hessian $\nabla^2 f_1$ is positive definite. Hence, $f_1(\mathbf{S})$ is strongly convex. □

Since problem (8) is convex with respect to $\mathbf{S}_{p\times n}$, a variety of optimization algorithms are applicable. In this work, the alternating direction method of multipliers (ADMM) [28] is employed. To facilitate optimization, a variable splitting is introduced as follows:

$$\begin{aligned} \min_{\mathbf{S},\mathbf{Z}} \quad & f_1(\mathbf{S}_{p\times n}) + f_2(\mathbf{Z}_{p\times n}) \\ s.t. \quad & \mathbf{S}_{p\times n} \geq \mathbf{0}_{p\times n}, \qquad \mathbf{S}_{p\times n} = \mathbf{Z}_{p\times n}, \end{aligned} \tag{9}$$

where $f_1(\mathbf{S}_{p\times n}) = \frac{1}{2}||\mathbf{Q}_p\mathbf{Y}_{p\times n} - \mathbf{S}_{p\times n}||_F^2 + \tau\sum_{j=1}^{n}\Big(\mathbf{1}_p^\top \mathbf{s}_j - 1\Big)^2$, $f_2(\mathbf{Z}_{p\times n}) = \mu||\mathbf{Z}_{p\times n}||_1$. The resulting alternating optimization procedure is then given by:

$$\begin{aligned} \mathbf{Z} &\leftarrow \min_{\mathbf{Z}} f_2(\mathbf{Z}) + \frac{\rho}{2}||\mathbf{S} - \mathbf{Z} + \mathbf{D}/\rho||_F^2 \\ \mathbf{S} &\leftarrow \min_{\mathbf{S}} f_1(\mathbf{S}) + \frac{\rho}{2}||\mathbf{S} - \mathbf{Z} + \mathbf{D}/\rho||_F^2 \\ \mathbf{D}^{k+1} &= \mathbf{D}^k - \Big(\mathbf{S}^{k+1} - \mathbf{Z}^{k+1}\Big), \end{aligned}$$

where $\mathbf{S}$ is the abundance matrix, ρ and $\mathbf{D}$ denote the penalty parameter and the Lagrange multiplier, respectively, in the augmented Lagrangian function.

It should be noted that the above way of splitting variables has two advantages. One is that the minimization of $\mathbf{S}$ has a closed-form solution. The other is that the minimization

of $\mathbf{Z}$ can be solved using the efficient soft-threshold method. More precisely, the iteration steps are as follows:

$$\mathbf{Z}^{k+1} = \max\left\{soft\left(\mathbf{S}^{k+1} - \mathbf{D}^k/\rho, \mu/\rho\right)\right\} \tag{10}$$

$$\mathbf{S}^{k+1} = \left(\mathbf{M}^\top\mathbf{M} + \rho\mathbf{I}_p + 2\tau\mathbf{1}_p\mathbf{1}_p{}^\top\right)^{-1} \left(\mathbf{M}^\top\mathbf{Y} + \rho\mathbf{Z}^k - \mathbf{D}^k + 2\tau\mathbf{1}_p\mathbf{1}_n^\top\right) \tag{11}$$

$$\mathbf{D}^{k+1} = \mathbf{D}^k - \left(\mathbf{S}^{k+1} - \mathbf{Z}^{k+1}\right), \tag{12}$$

where $soft(\cdot, \theta)$ denotes the component-wise application of the soft-threshold function, i.e., $soft(x, \theta) = sign(x)max\{|x| - \theta, 0\}$. Set $resp^k = ||\mathbf{S}_k - \mathbf{Z}_k||_F^2$, $resd^k = ||\mathbf{Z}_k - \mathbf{Z}_{k-1}||_F^2$. The proposed L_1_SoftASC algorithm used in Stage II is summarized in Algorithm 2.

Algorithm 2 Second Stage: ADMM for the L_1-SoftASC Model

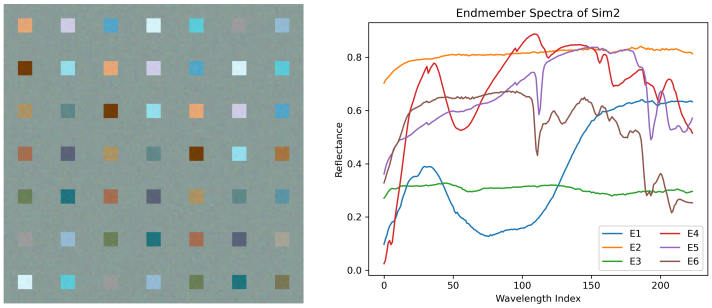
1: **Input:** Q^*; parameters $\tau = 10^{-1}$, $\mu = 10^{-4}$, $\rho = 10^{-3}$; stopping tolerances $\eta_1 = 10^{-2}$ and $\eta_2 = 10^{-2}$; primal and dual residuals are $resp^1 = 1$, $resd^1 = 1$; $k \leftarrow 1$
2: **Initialize:** $\mathbf{D}^0 = \mathbf{0}$; $\mathbf{S}^0 = \mathbf{Z}^0 = \text{Proj}(Q^*)$ [14];
3: **while** $resp^k \geq \eta_1$ **or** $resd^k \geq \eta_2$ **do**
4: Update $\mathbf{Z}^k$ according to (10)
5: Update $\mathbf{S}^k$ according to (11)
6: Update $\mathbf{D}^k$ according to (12)
7: Compute the primal residual $resp^{k+1}$ and dual residual $resd^{k+1}$
8: $k \leftarrow k + 1$
9: **end while**
10: **Output:** $\mathbf{S}^*$, $\mathbf{Z}^*$, and $\mathbf{D}^*$

4. Results and Discussion

4.1. Datasets

- Simulated datasets [4]: Sim1 and Sim2

Both datasets contain 105×105 pixels, generated by linear mixtures of the same six endmembers, with no pure pixels in either dataset. These endmembers contain 224 reflection values in the wavelength ranging from 400 nm to 2500 nm. The main difference between them is that Sim1 has at least two mixed data points on each facet to geometrically reconstruct virtual endmembers, whereas Sim2 has only one. Each dataset includes three signal-to-noise ratio (SNR) levels in dB: 20, 30, and 40. The Sim2_SNR40 dataset is shown in Figure 3.



(**a**) Sim2_SNR40 (**b**) Truth Endmembers

Figure 3. Sim2_SNR40 dataset description.

- Benchmark real-world datasets [9,29]: Samson, Jasper Ridge (JR), Washington DC Mall (WDC) and Cuprite

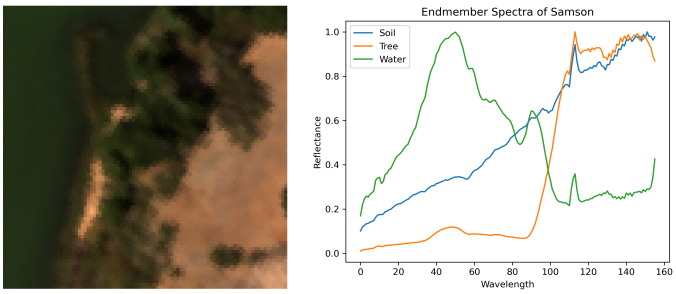
The Samson dataset consists of 95 × 95 pixels, each with 156 spectral bands ranging from 401 nm to 889 nm. It includes three primary endmembers: soil, tree, and water.

The Jasper Ridge dataset has 100 × 100 pixels, each with selected 198 bands ranging from 380 nm to 2500 nm. There are four main endmembers, i.e., soil, tree, road and water.

The Washington DC Mall (WDC) dataset contains 319 × 292 pixels, each with 191 spectral bands spanning from 400 nm to 2400 nm. Six major endmembers are identified: grass, tree, road, roof, water, and trail.

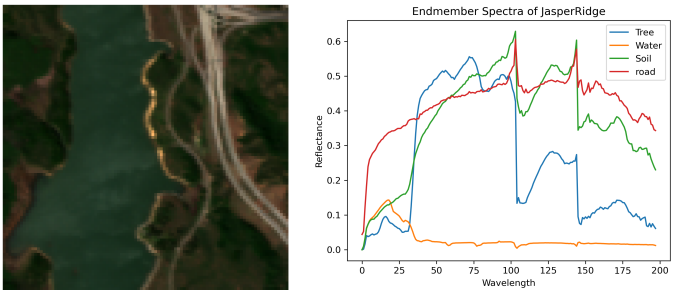
The Cuprite dataset is a 250 × 190 subimage acquired by the AVIRIS sensor over the Cuprite mining district near Las Vegas, Nevada, USA. The scene is mainly composed of mineral materials, with up to 14 minerals estimated in this area. The raw data contain 224 spectral bands covering the wavelength range from 400 nm to 2500 nm. Following common settings in the literature [9], 188 clean bands are selected, and 12 representative endmembers are considered, i.e., Alunite, Andradite, Buddingtonite, Dumortierite, Kaolinite_1, Kaolinite_2, Muscovite, Montmorillonite, Nontronite, Pyrope, Sphene, and Chalcedony. To the best of our knowledge, there is currently no publicly available ground-truth abundance data.

The pseudo-RGB images and ground-truth endmembers for the Samson, Jasper Ridge, WDC datasets are shown in Figure 4, Figure 5, and Figure 6, respectively. A mineral map of Cuprite mining district provided by USGS in 1995 is shown in Figure 7a and ground-truth endmembers are shown in Figure 7b.



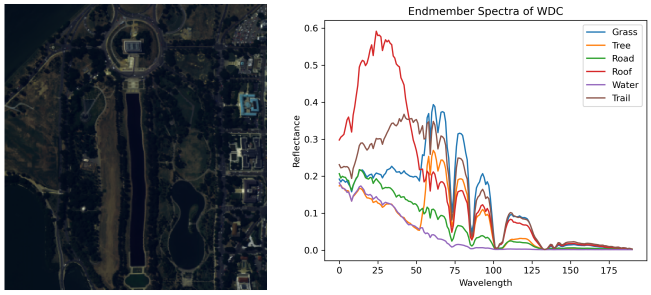
(**a**) Samson (**b**) Ground truth endmembers

Figure 4. Samson dataset description.



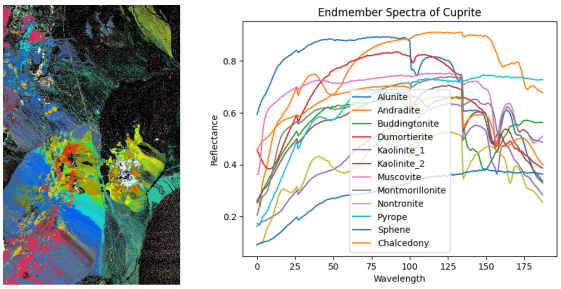
(**a**) Jasper Ridge (**b**) Ground truth endmembers

Figure 5. Jasper Ridge dataset description.



(**a**) WDC (**b**) Ground truth endmembers

Figure 6. WDC dataset description.



(**a**) Cuprite (**b**) Ground truth endmembers

Figure 7. Cuprite dataset description.

4.2. Baseline Algorithms

All baseline algorithms used in this study are publicly available from the sources cited in their respective publications. Most methods were evaluated using the default parameters provided in their official implementations. For some methods, we further tuned key hyperparameters based on their default values and parameter meanings in order to obtain better performance.

For endmember extraction, the following four categories of methods are compared:

1. Minimum-volume-based methods (MV-Un): SISAL [23], QMVNMF [7], and the proposed CMV [24];
2. Geometrical methods (Geo-Un): VCA [30];
3. NMF-based methods: SeCoDe [21], EDAA [29];
4. Deep learning-based methods (DL): MiSiC [4], A2SN [31], DFFN [32].

Among them, QMVNMF and CMV can be classified as both MV-based and NMF-based approaches, while MiSiC can be categorized as both DL-based and MV-based.

For abundance inversion, two groups of methods are evaluated: SSMs and TSMs. Since the concept of TSMs is introduced in this paper for the first time for NMF-based methods, the existing approaches have not previously been defined as two-stage methods. As SISAL and VCA are classical endmember extraction algorithms, we design three types of TSM combinations (SISAL+Proj, SISAL+L_1, VCA+Proj, VCA+L_1, CMV+Proj, and CMV+L_1) to compare the performance of each stage and the overall performance. In addition, since A2SN employs a network that first recovers abundances and then estimates endmembers without interactive updates, we include this method in the TSM category.

1. SSMs: QMVNMF, SeCoDe, and EDAA;
2. TSMs: SISAL+Proj, SISAL+L_1, VCA+Proj, VCA+L_1, CMV+Proj, CMV+L_1 and A2SN [31].

Here, "Proj" refers to abundance estimation via projection onto the simplex [14], while "L_1" denotes the proposed L_1_SoftASC method (see Algorithm 2 for details). To evaluate

performance, the spectral angle distance (SAD) and root mean square error (RMSE) are used to assess endmember and abundance estimation accuracy, respectively, as defined below:

$$SAD(\mathbf{M}, \hat{\mathbf{M}}) := 1/p \sum_{i=1}^{p} \arccos\left(\frac{\mathbf{m}_i^T \hat{\mathbf{m}}_i}{\|\mathbf{m}_i\| \|\hat{\mathbf{m}}_i\|}\right) \frac{180}{\pi},$$

$$RMSE(\mathbf{S}, \hat{\mathbf{S}}) = \frac{100 \times \|\mathbf{S} - \hat{\mathbf{S}}\|_F}{\sqrt{p \times N}}.$$

4.3. Experimental Results

As shown in Tables 1 and 2, the proposed CMV method achieves the highest overall endmember accuracy, as measured by SAD. This further validates the effectiveness of minimum-volume (MV) methods combined with strong convex regularization for endmember extraction. In addition, methods incorporating volume regularization terms, such as QMVNMF and MiSiC, also achieve overall competitive performance. The estimated endmembers for Sim2, Samson, Jasper Ridge, WDC, and Cuprite obtained by different algorithms are visualized in Figure 8, Figure 9, Figure 10, Figure 11, and Figure 12, respectively.

Table 1. The comparison of SAD (in degrees) for simulated and real datasets.

Datasets	MV-Un			Geo-Un	NMF		DL		
	SISAL	**QMVNMF**	**CMV (Proposed)**	**VCA**	**SeCoDe**	**EDAA**	**MiSiC**	**A2SN**	**DFFN**
Sim 1 SNR40	0.64	0.58	**0.13**	6.84	19.46	13.83	0.61	10.96	9.35
Sim 1 SNR30	2.13	0.55	**0.47**	4.45	13.81	13.83	1.03	10.90	8.87
Sim 1 SNR20	14.77	**2.00**	2.23	5.34	17.18	13.91	3.45	10.85	9.35
Sim 2 SNR40	0.56	10.86	**0.12**	11.70	10.96	16.04	0.64	10.94	8.98
Sim 2 SNR30	2.23	2.92	**0.38**	7.37	22.45	15.15	0.80	10.89	10.32
Sim 2 SNR20	13.74	8.55	2.20	6.38	16.58	14.29	**1.73**	10.86	12.21
Samson_Soil	7.91	1.23	0.98	0.97	1.45	**0.49**	0.59	1.01	3.41
Samson_Tree	6.26	1.75	**0.30**	2.52	2.37	1.96	2.03	2.27	1.98
Samson_Water	16.94	1.52	**0.62**	7.12	1.68	1.04	22.98	6.64	2.69
Samson_Overall	10.37	1.50	**0.63**	3.54	1.83	1.16	8.54	3.31	2.69
JR_Tree	17.55	4.54	**3.57**	11.09	3.68	4.07	2.48	5.50	5.10
JR_Water	19.39	19.39	1.87	14.64	**1.72**	2.93	16.62	6.92	8.24
JR_Soil	33.59	1.85	**1.38**	6.37	7.82	2.59	3.80	4.76	10.68
JR_Road	42.76	3.03	**2.67**	3.18	39.21	4.17	18.89	10.34	6.31
JR_Overall	28.32	7.20	**2.37**	8.82	13.11	3.44	10.45	6.88	7.58
WDC_Grass	25.26	6.74	**3.91**	11.48	9.68	14.79	10.97	13.22	10.60
WDC_Tree	28.57	18.50	**1.82**	16.09	14.85	15.94	8.59	6.05	17.19
WDC_Road	30.88	5.80	6.44	13.95	15.75	36.33	**5.11**	12.01	11.76
WDC_Roof	34.90	17.84	**14.51**	20.17	38.02	22.32	19.01	19.99	18.81
WDC_Water	55.73	1.74	2.11	22.05	2.88	**1.19**	2.49	4.58	25.96
WDC_Trail	56.39	**2.24**	23.76	10.29	10.94	16.43	32.64	38.25	18.57
WDC_Overall	38.62	8.81	**8.76**	15.67	15.35	17.83	13.14	15.68	17.15

Note: The best value in each row is highlighted in bold.

In the second stage of TSMs, the evaluated methods are grouped into three sets, each sharing the same endmembers.

1. SISAL+Proj vs. SISAL+L_1
2. VCA+Proj vs. VCA+L_1
3. CMV+Proj vs. CMV+L_1

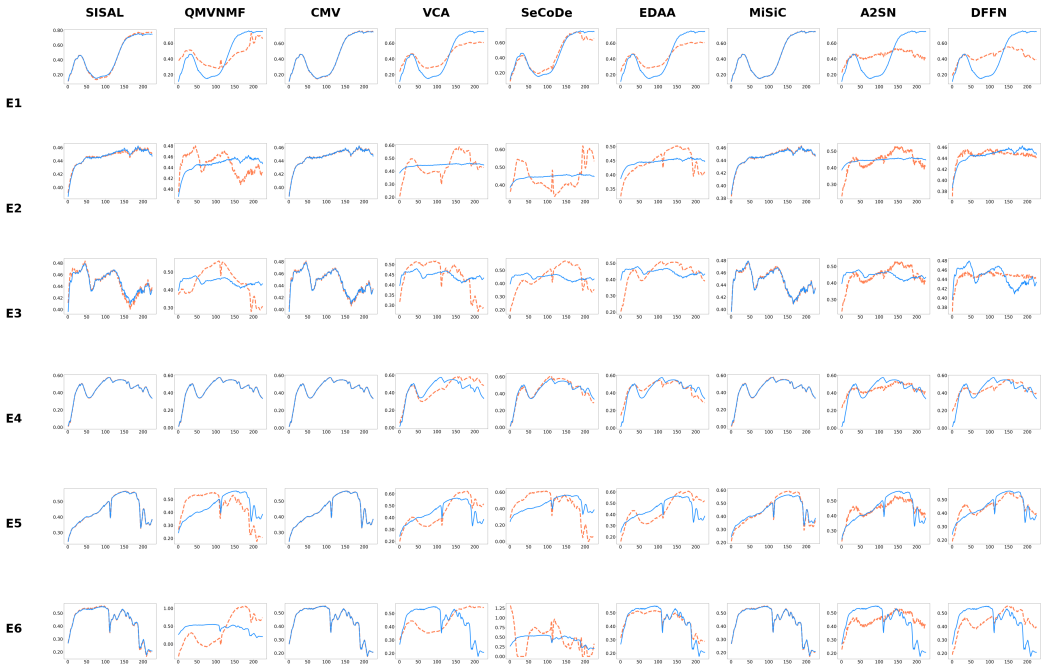


Figure 8. Sim2_SNR40_Endmembers. The visual comparison of the endmembers obtained by the different unmixing techniques. Blue: ground-truth endmembers. Orange: estimated endmembers.

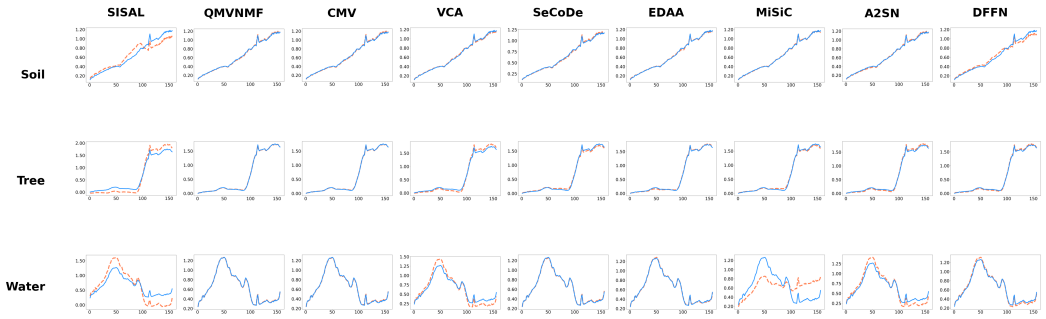


Figure 9. Samson_Endmembers. The visual comparison of the endmembers obtained by the different unmixing techniques. Blue: ground-truth endmembers. Orange: estimated endmembers.

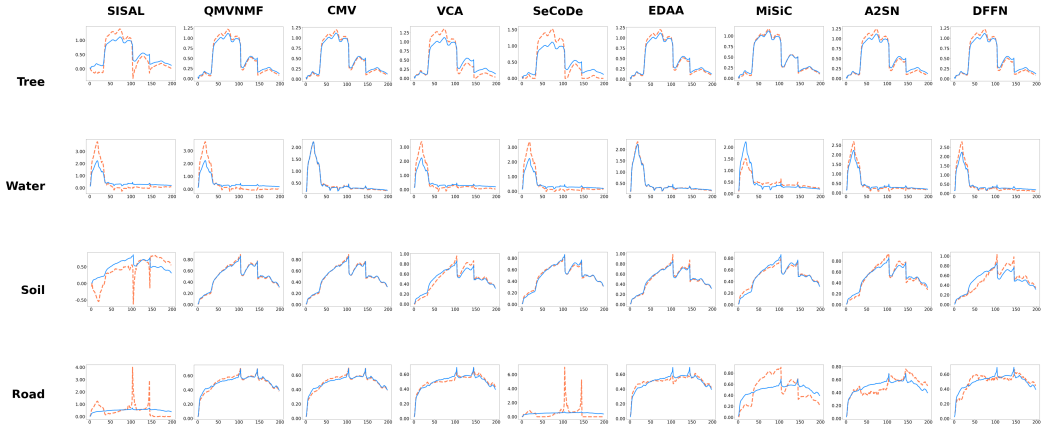


Figure 10. Jasper Ridge_Endmembers. The visual comparison of the endmembers obtained by the different unmixing techniques. Blue: ground-truth endmembers. Orange: estimated endmembers.

As presented in Table 3, the proposed CMV+L_1 method attains the best overall abundance estimation accuracy measured by RMSE across all datasets. QMVNMF achieves the second-best performance overall, while EDAA demonstrates competitive results on the

Samson and Jasper Ridge datasets. The corresponding abundance maps are visualized in Figure 13, Figure 14, Figure 15, Figure 16, and Figure 17, respectively.

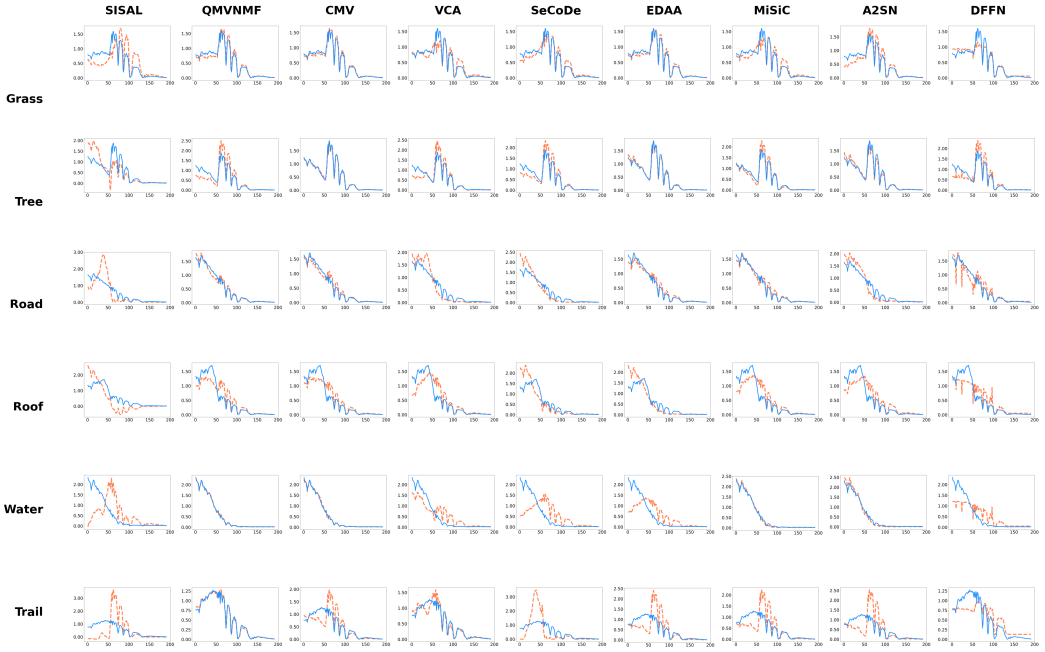


Figure 11. WDC_Endmembers. The visual comparison of the endmembers obtained by the different unmixing techniques. Blue: ground-truth endmembers. Orange: estimated endmembers.

Table 2. The comparison of SAD (in degrees) for Cuprite dataset.

Cuprite	MV-Un			Geo-Un	NMF		DL		
	SISAL	**QMVNMF**	**CMV (Proposed)**	**VCA**	**SeCoDe**	**EDAA**	**MiSiC**	**A2SN**	**DFFN**
Alunite	12.73	5.35	**4.68**	5.95	8.41	13.64	8.62	9.91	6.25
Andradite	14.89	4.38	4.27	**3.83**	8.76	4.83	4.49	5.07	4.26
Buddingtonite	16.75	6.98	7.21	**4.56**	8.66	7.44	6.66	6.96	5.72
Dumortierite	13.42	6.19	5.59	5.76	11.10	8.00	9.24	5.56	**4.61**
Kaolinite_1	11.04	5.72	6.41	**4.48**	15.95	6.93	7.97	9.70	6.48
Kaolinite_2	18.80	4.60	4.24	5.52	15.33	4.01	11.43	**3.91**	4.24
Muscovite	22.47	9.93	10.34	8.33	16.59	9.02	13.71	7.49	**4.19**
Montmorillonite	18.73	8.00	6.12	5.18	19.64	**3.67**	11.73	5.11	7.98
Nontronite	22.91	7.61	6.65	**4.13**	20.15	4.43	12.47	7.06	8.29
Pyrope	22.76	4.78	4.49	4.97	23.69	8.03	13.65	17.28	**3.58**
Sphene	40.51	6.97	**3.73**	20.68	31.31	10.94	15.30	55.32	25.47
Chalcedony	80.64	73.44	67.01	63.78	67.08	60.64	57.47	62.93	**56.95**
Overall	24.64	12.00	**10.90**	11.43	20.56	11.80	14.39	16.36	11.50

Note: The best value in each row is highlighted in bold.

From these figures, it can be observed that SISAL+L_1 consistently outperforms SISAL+Proj. The same trend is also observed for VCA+L_1 versus VCA+Proj, and for CMV+L_1 versus CMV+Proj. Within each comparison group, the L_1-based method yields significantly better abundance accuracy than the Proj method, indicating that, for the same endmember estimates, SoftASC is more accurate than hard ASC.

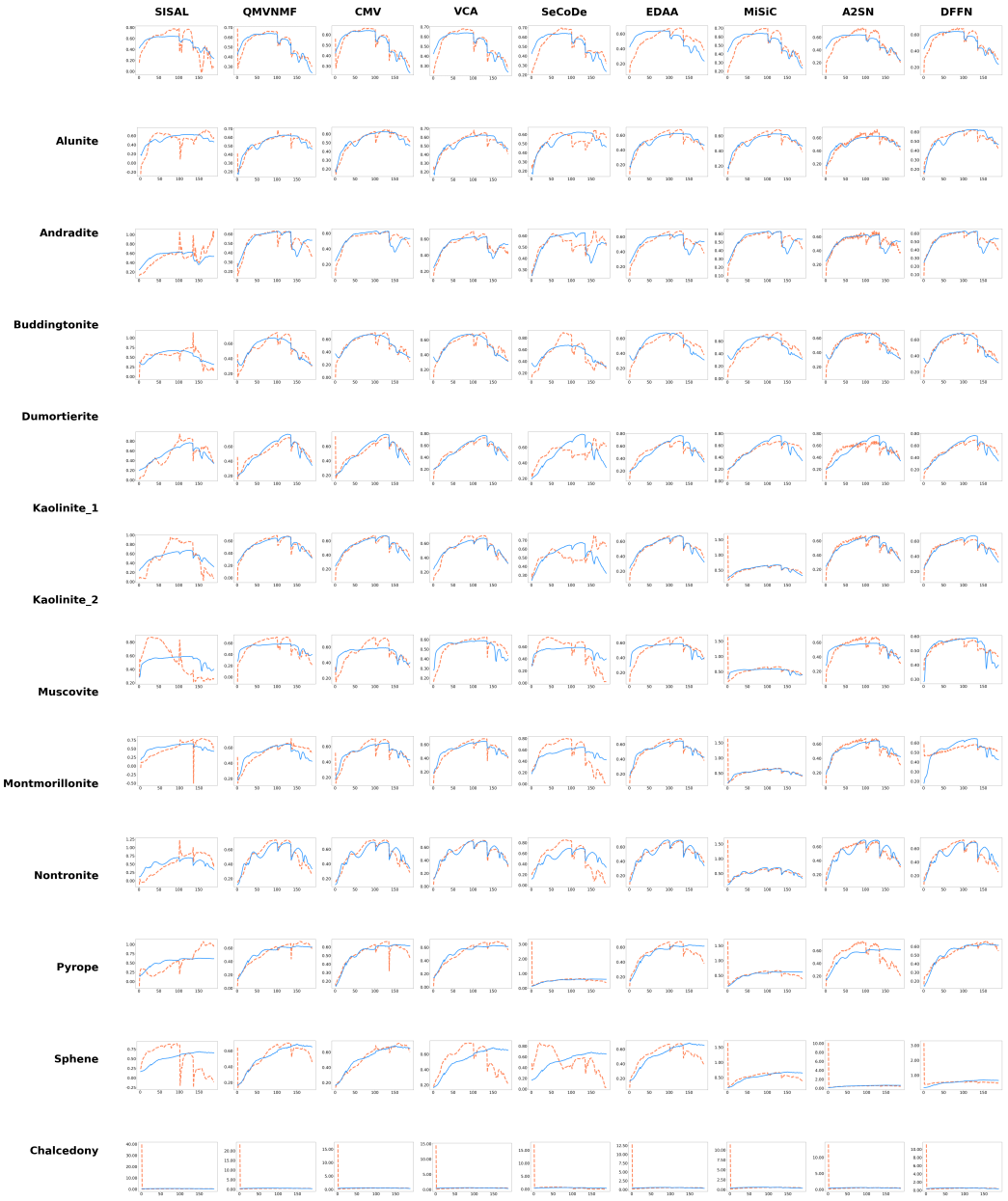


Figure 12. Cuprite_Endmembers. The visual comparison of the endmembers obtained by the different unmixing techniques. Blue: ground-truth endmembers. Orange: estimated endmembers.

These figures also enable a comparison between the NMF-based SSMs and the proposed TSMs. The SSMs exhibit an inherent trade-off between endmember accuracy and abundance accuracy. For example, although QMVNMF and SeCoDe achieve reasonable endmember accuracy on the Samson dataset, they fail to produce competitive abundance estimates. Attempts to tune the parameters for improved abundance performance often compromise endmember accuracy, further reflecting the strong coupling between these two components in SSMs.

In summary, the proposed CMV+L_1 method consistently achieves the best overall performance in terms of both SAD and RMSE. For the same endmember estimates, SoftASC provides a more reasonable and accurate abundance model. More importantly, the TSMs offer the capability for decoupled optimization of endmembers and abundances, whereas such flexibility is inherently limited in SSM-based approaches.

Table 3. The comparison of RMSE for simulated and real datasets.

Datasets	SSM					TSM						
	QMVNMF	SeCoDe	EDAA	MiSiC	DFFN	SISAL +proj	SISAL +L_1	VCA +proj	VCA +L_1	CMV +proj	A2SN	CMV+L_1 (Proposed)
Sim 1 SNR40	1.00	35.54	12.67	11.85	18.01	1.76	0.59	12.89	6.68	1.75	8.31	**0.40**
Sim 1 SNR30	2.28	34.94	12.70	10.65	18.62	4.81	1.59	7.77	6.16	5.01	9.73	**1.23**
Sim 1 SNR20	3.70	34.71	11.13	10.67	19.15	10.63	7.46	13.28	7.31	10.49	10.60	**3.54**
Sim 2 SNR40	3.96	24.27	8.34	2.14	21.92	1.74	0.54	17.86	7.63	1.74	8.37	**0.40**
Sim 2 SNR30	2.01	34.66	12.57	10.54	18.14	4.73	1.79	12.21	7.18	5.09	10.14	**1.21**
Sim 2 SNR20	4.14	33.56	12.61	9.09	16.05	10.36	7.89	16.29	11.23	9.91	9.81	**3.46**
Samson_Soil	7.82	18.92	5.35	17.91	5.25	12.52	15.23	13.11	7.11	7.45	6.96	**2.90**
Samson_Tree	7.39	22.00	**3.57**	18.19	4.88	12.92	14.58	10.09	7.31	7.21	4.62	4.05
Samson_Water	2.68	18.77	1.96	31.31	2.12	12.31	4.51	8.31	8.15	2.43	5.35	**1.49**
Samson_Overall	6.40	19.95	3.88	23.32	4.32	12.58	12.45	10.69	7.53	6.15	5.73	**3.00**
JR_Tree	11.51	8.33	6.03	9.59	9.82	18.25	18.27	12.62	12.07	10.51	9.91	**4.27**
JR_Water	8.97	10.49	7.73	11.43	8.17	25.00	25.09	8.73	6.42	10.55	12.30	**4.86**
JR_Soil	8.96	24.66	**5.97**	22.13	13.80	25.67	25.35	12.53	12.73	7.97	9.66	8.77
JR_Road	8.78	23.64	7.42	24.93	12.54	24.67	24.64	7.80	8.23	7.29	11.71	**6.28**
JR_Overall	9.62	18.35	6.83	18.26	11.30	23.59	23.52	10.65	10.21	9.20	10.95	**6.29**
WDC_Grass	33.72	43.36	54.71	31.19	53.08	38.51	28.59	40.96	33.20	33.76	31.64	**22.56**
WDC_Tree	28.14	40.64	35.63	33.17	**14.33**	27.52	30.84	27.38	27.61	27.04	35.95	17.45
WDC_Road	22.91	21.85	39.97	35.33	**14.13**	21.76	23.30	28.03	25.87	34.01	25.51	19.63
WDC_Roof	11.48	**6.93**	18.89	34.97	25.47	22.66	17.06	17.04	12.00	35.66	28.13	26.10
WDC_Water	14.46	16.45	**10.22**	35.24	43.40	40.34	43.30	41.16	30.18	38.71	41.39	16.22
WDC_Trail	9.92	**8.40**	24.06	34.08	41.89	30.21	19.96	23.79	14.24	17.19	48.23	24.21
WDC_Overall	21.93	27.08	20.39	34.03	35.38	31.00	28.51	30.99	25.14	31.87	36.00	**18.30**

Note: The best value in each row is highlighted in bold.

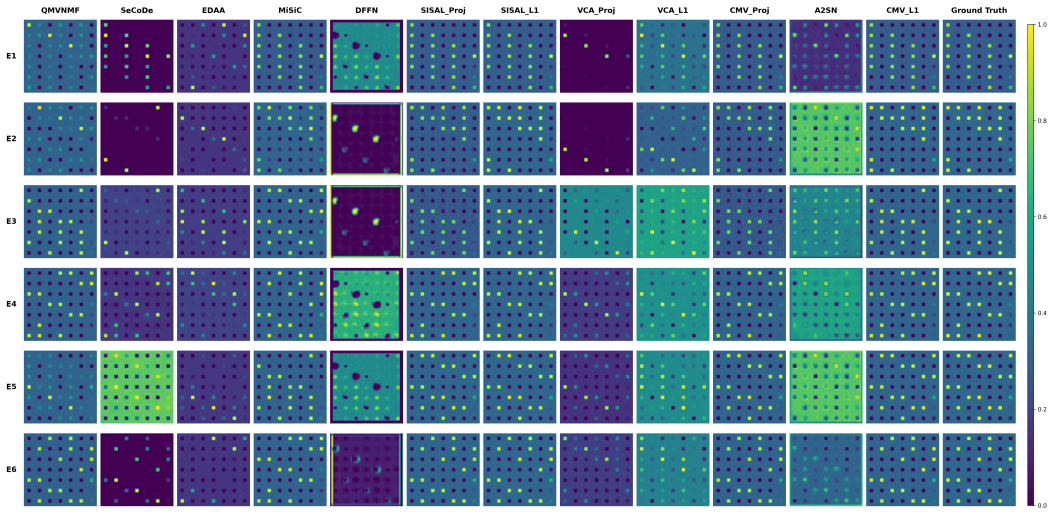


Figure 13. Sim2_SNR40_Abundance Maps. The visual comparison of the abundance maps obtained by the different unmixing techniques.

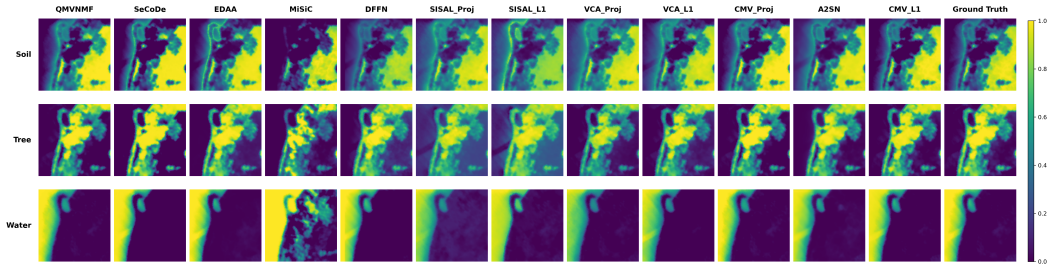


Figure 14. Samson_Abundance maps. The visual comparison of the abundance maps obtained by the different unmixing techniques.

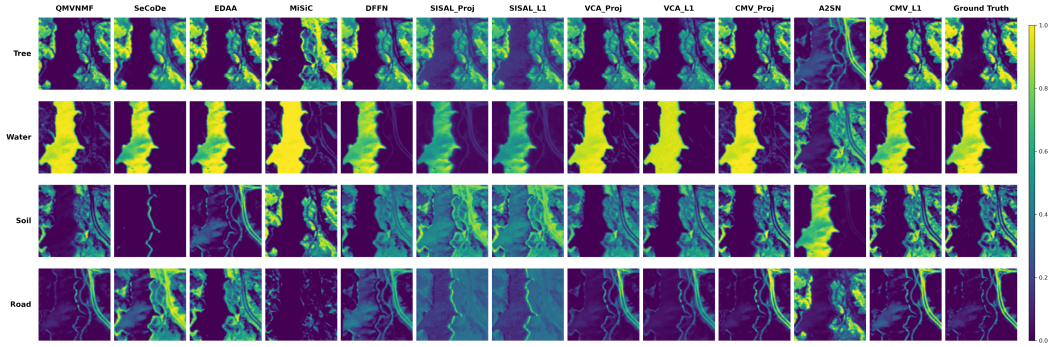


Figure 15. Jasper Ridge_Abundance maps. The visual comparison of the abundance maps obtained by the different unmixing techniques.

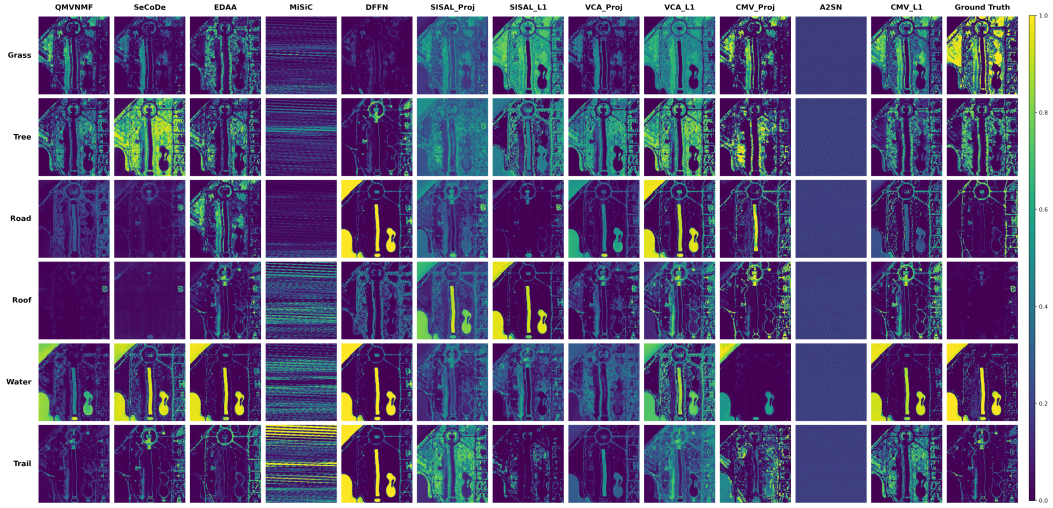


Figure 16. WDC_Abundance maps. The visual comparison of the abundance maps obtained by the different unmixing techniques.

4.4. Initial Robustness

As previously noted, the proposed CMV model for endmember extraction is strongly convex and therefore exhibits initial robustness on endmembers, as demonstrated in [24]. Similarly, the proposed L_1 method is also strongly convex, providing robustness to abundance initialization.

All baseline algorithms require predefined initial points, which are summarized in Table 4. In this context, "ATGP" refers to the abundance-unconstrained Automatic Target Generation Process [33]. The EDAA method adopts specific initializations as outlined in its original paper [29], while CMV utilizes randomly generated initial points, following the design in [24].

Table 4. Initial points of baseline algorithms.

algorithms	VCA	SISAL	QMV-NMF	SeCoDe	EDAA	CMV
initial method	ATGP	VCA	VCA	VCA	specific	random

4.5. Convergence and Computational Complexity

In the first stage, the proposed CMV model is smooth, gradient-Lipschitz continuous, and strongly convex, as established in [26] and is solved by Algorithm 1 (Adam + Proj). Adam is an adaptive first-order optimization method that avoids the need to compute the Hessian matrix. Under the aforementioned conditions, Adam guarantees a linear conver-

gence rate. The primary computational costs arise from the matrix multiplication $\mathbf{Q}_p\mathbf{Y}_{p\times n}$ and Proj($\mathbf{Q}_p\mathbf{Y}_{p\times n}$), with computational complexities $O(p^2n)$ and $O(nplogp)$, respectively.

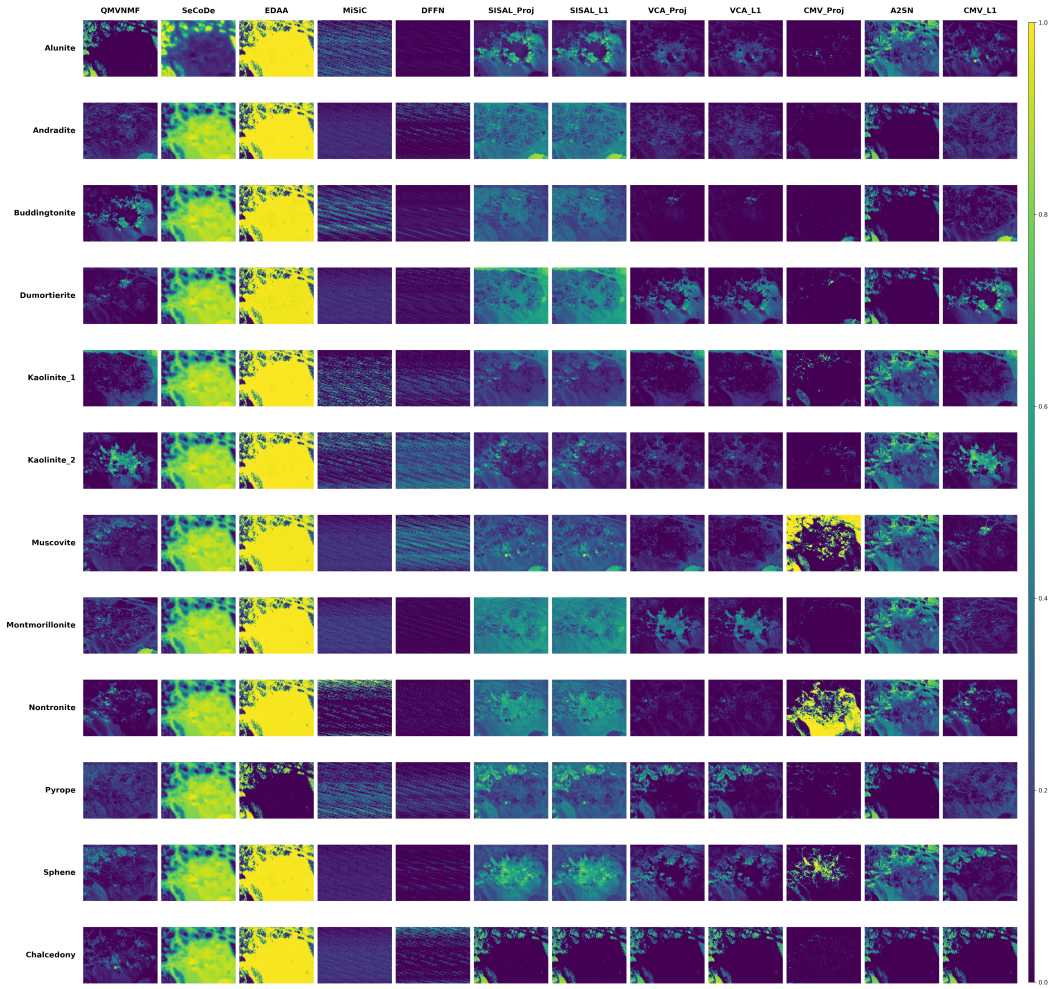


Figure 17. Cuprite_Abundance maps. The visual comparison of the abundance maps obtained by the different unmixing techniques.

In the second stage, we employ the ADMM, with variable splitting introduced in (9). ADMM guarantees global convergence because the following conditions are satisfied: (a) both $f_1(\mathbf{S}_{p\times n})$ and $f_2(\mathbf{Z}_{p\times n})$ in Equation (9) are proper, closed, and convex functions; (b) the equality constraint $\mathbf{S}_{p\times n} = \mathbf{Z}_{p\times n}$ is affine. Notably, the $\mathbf{S}$-subproblem admits a closed-form solution. Furthermore, the strong convexity of $f_1(\mathbf{S}_{p\times n})$ ensures linear convergence rate of ADMM iterations [34].

Based on the ideal properties of smoothness, gradient Lipschitz continuity, and strong convexity, a wide range of efficient optimization algorithms can be employed, including parallel implementations and acceleration techniques.

From the perspective of parameter tuning, the proposed two-stage model is easier to handle in practice. As shown in Figure 2, NMF-based JOP models usually involve at least three parameters together with two coupled matrix variables. In practice, optimization methods such as ADAM are often adopted, and the variables may be further split into several subvariables (for example, five variables in some implementations such as SUNSAL-TV). Although each subproblem is single-variable and relatively easy to solve, the overall optimization process still involves coupled matrix variables, which makes parameter tuning more difficult due to the coupling effect.

By contrast, in the proposed two-stage framework, the first stage involves only one main parameter and is therefore relatively easy to tune. In the second stage, there are two main parameters: one controls sparsity, while the other controls the degree of deviation from ASC. As shown in Section 4.7, a moderately small value of the SoftASC parameter is usually sufficient to achieve better performance than hard ASC. In this sense, the second stage is also practically manageable, since only one key parameter requires careful tuning. Overall, each stage in the proposed framework contains only one or two parameters to tune, while avoiding the coupling effect. Therefore, compared with single-stage joint optimization methods, the two-stage framework remains practical in terms of parameter tuning.

4.6. Ablation Analysis

We first examine the effect of different endmember extraction methods used in the first stage. As shown in Table 5, when the same abundance inversion process (H-ASC, SoftASC, or No ASC) is adopted, the proposed CMV method significantly outperforms SISAL and VCA in terms of abundance accuracy. This observation indicates that accurate endmember estimation is essential for the second stage.

Table 5. RMSE comparison under different ASC settings.

Simulated Datasets	SISAL+L_1			VCA+L_1			CMV+L_1		
	H-ASC	**SoftASC**	**No ASC**	**H-ASC**	**SoftASC**	**No ASC**	**H-ASC**	**SoftASC**	**No ASC**
Sim 1 SNR40	1.76	**0.59**	1.74	12.89	**6.68**	6.74	1.75	**0.40**	1.68
Sim 1 SNR30	4.81	**1.59**	4.02	7.77	**6.16**	6.72	5.01	**1.23**	3.94
Sim 1 SNR20	10.63	**7.46**	9.87	13.28	**7.31**	7.84	10.49	**3.54**	8.04
Sim 2 SNR40	1.74	**0.54**	1.70	17.86	**7.63**	19.03	1.74	**0.40**	1.66
Sim 2 SNR30	4.73	**1.79**	4.12	12.21	**7.18**	7.19	5.09	**1.21**	3.90
Sim 2 SNR20	10.36	**7.89**	9.95	16.29	**11.23**	11.36	9.91	**3.46**	7.93

Note: The best value in each row is highlighted in bold.

In the second stage, we further analyze the effect of SoftASC. Specifically, we consider the following three cases for ASC:

(1) SISAL+L_1+H-ASC, where H-ASC denotes hard ASC;
(2) SISAL+L_1+SoftASC;
(3) SISAL+L_1 No ASC.

Note that SISAL+L_1+hard ASC is in fact equivalent to SISAL+ hard ASC, since under hard ASC the L_1 norm becomes a constant. Although L_1 regularization is widely used to promote sparsity, the presence of hard ASC renders the L_1 term ineffective, which is why hard ASC is often omitted in practice. Our results show that the proposed combination of L_1 regularization and SoftASC significantly outperforms the use of L_1 regularization alone. As reported in Table 5, incorporating SoftASC consistently improves abundance estimation accuracy for all tested endmember extraction methods, including SISAL, VCA, and CMV.

4.7. Sensitivity Analysis of SoftASC Parameters

The previous sections have shown that the hard ASC is inconsistent with noisy scenarios, leading to degraded abundance estimation accuracy. In this section, we further investigate the influence of the SoftASC weight parameter τ on abundance estimation accuracy, measured by RMSE. To ensure fairness and comparability across datasets, we used the same parameter settings for all datasets and report results averaged over 10 independent runs. In addition, the L_1-norm term was omitted so that the effect of SoftASC on RMSE could be examined in isolation.

When $\tau = 0$, only the nonnegativity constraint is imposed, whereas larger values of τ impose stronger penalties on deviations from the ASC. Figure 18 presents the RMSE as a function of τ under different SNR levels for both synthetic and real datasets. Across all datasets, moderate soft-constraint levels, e.g., $\tau \in (10^{-3}, 10^{-2})$, consistently lead to improved abundance estimation accuracy, indicating that SoftASC provides an effective trade-off between model flexibility and constraint enforcement.

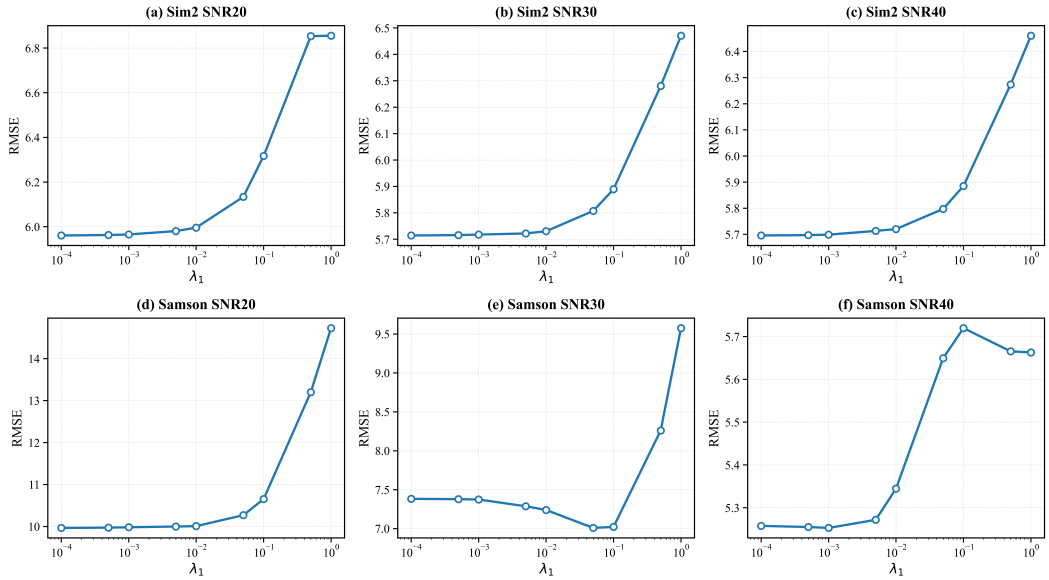


Figure 18. SoftASC parameters vs. RMSE.

5. Conclusions

In NMF-based JOPs for LHU the coupling between endmembers and abundances is an inherent limitation. This paper introduces a new decoupling perspective to separately refining endmember and abundance accuracy. We have demonstrated that, given the same endmember estimates, abundance estimation accuracy can be independently improved in the second stage. However, how to incorporate spatial information to further improve abundance estimation accuracy still requires further investigation. In addition, although our experiments show that a moderate SoftASC parameter can improve accuracy compared with hard ASC, accurate or adaptive parameter selection remains an important direction for future research.

Author Contributions: Conceptualization, Y.L. and H.L.; methodology, Y.L.; software, Y.L.; validation, H.L. and X.C.; formal analysis, Y.W. and Y.Z.; writing—original draft preparation, Y.L.; writing—review and editing, Y.L.; visualization, H.L.; supervision, Y.W. and Y.Z.; funding acquisition, Y.W. All authors have read and agreed to the published version of the manuscript.

Funding: This research was funded by the National Natural Science Foundation of China Joint Fund Project Key Support Project, grant number U22B2049, awarded to Yongli Wang.

Data Availability Statement: All data used in this paper can be downloaded from the following websites: https://github.com/inria-thoth/EDAA (accessed on 14 January 2026), https://github.com/BehnoodRasti/MiSiCNet (accessed on 14 January 2026).

Conflicts of Interest: The authors declare no conflicts of interest.

References

1. Jia, S.; Qian, Y. Spectral and Spatial Complexity-Based Hyperspectral Unmixing. *IEEE Trans. Geosci. Remote Sens.* **2007**, *45*, 3867–3879. [CrossRef]
2. Feng, X.R.; Li, H.C.; Wang, R.; Du, Q.; Jia, X.; Plaza, A. Hyperspectral Unmixing Based on Nonnegative Matrix Factorization: A Comprehensive Review. *IEEE J. Sel. Top. Appl. Earth Obs. Remote Sens.* **2022**, *15*, 4414–4436. [CrossRef]
3. Bhatt, J.S.; Joshi, M.V.; Raval, M.S. A Data-Driven Stochastic Approach for Unmixing Hyperspectral Imagery. *IEEE J. Sel. Top. Appl. Earth Obs. Remote Sens.* **2014**, *7*, 1936–1946. [CrossRef]
4. Rasti, B.; Koirala, B.; Scheunders, P.; Chanussot, J. MiSiCNet: Minimum Simplex Convolutional Network for Deep Hyperspectral Unmixing. *IEEE Trans. Geosci. Remote Sens.* **2022**, *60*, 5522815. [CrossRef]
5. Rasti, B.; Koirala, B. SUnCNN: Sparse Unmixing Using Unsupervised Convolutional Neural Network. *IEEE Geosci. Remote Sens. Lett.* **2022**, *19*, 5508205. [CrossRef]
6. Shao, Y.; Liu, Q.; Xiao, L. IVIU-Net: Implicit Variable Iterative Unrolling Network for Hyperspectral Sparse Unmixing. *IEEE J. Sel. Top. Appl. Earth Obs. Remote Sens.* **2023**, *16*, 1756–1770. [CrossRef]
7. Zhuang, L.; Lin, C.H.; Figueiredo, M.A.T.; Bioucas-Dias, J.M. Regularization Parameter Selection in Minimum Volume Hyperspectral Unmixing. *IEEE Trans. Geosci. Remote Sens.* **2019**, *57*, 9858–9877. [CrossRef]
8. Bioucas-Dias, J.; Figueiredo, M. Alternating Direction Algorithms for Constrained Sparse Regression: Application to Hyperspectral Unmixing. *arXiv* **2010**, arXiv:1002.4527.
9. Iordache, M.D.; Bioucas-Dias, J.M.; Plaza, A. Total Variation Spatial Regularization for Sparse Hyperspectral Unmixing. *IEEE Trans. Geosci. Remote Sens.* **2012**, *50*, 4484–4502. [CrossRef]
10. Chen, L.; Chen, S.; Guo, X. Multilayer NMF for Blind Unmixing of Hyperspectral Imagery with Additional Constraints. *Photogramm. Eng. Remote Sens.* **2017**, *83*, 307–316. [CrossRef]
11. Xiong, F.; Zhou, J.; Tao, S.; Lu, J.; Qian, Y. SNMF-Net: Learning a Deep Alternating Neural Network for Hyperspectral Unmixing. *IEEE Trans. Geosci. Remote Sens.* **2021**, *60*, 5510816. [CrossRef]
12. Xiong, F.; Zhou, J.; Ye, M.; Lu, J.; Qian, Y. NMF-SAE: An Interpretable Sparse Autoencoder for Hyperspectral Unmixing. In Proceedings of the ICASSP 2021—2021 IEEE International Conference on Acoustics, Speech and Signal Processing (ICASSP), Toronto, ON, Canada, 6–11 June 2021. [CrossRef]
13. Heylen, R.; Burazerovic, D.; Scheunders, P. Fully Constrained Least Squares Spectral Unmixing by Simplex Projection. *IEEE Trans. Geosci. Remote Sens.* **2011**, *49*, 4112–4122. [CrossRef]
14. Wang, W.; Carreira-Perpiñán, M.A. Projection onto the probability simplex: An efficient algorithm with a simple proof, and an application. *arXiv* **2013**, arXiv:1309.1541. . [CrossRef]
15. Shen, X.; Chen, L.; Liu, H.; Su, X.; Wei, W.; Zhu, X.; Zhou, X. Efficient Hyperspectral Sparse Regression Unmixing With Multilayers. *IEEE Trans. Geosci. Remote Sens.* **2023**, *61*, 5522614. [CrossRef]
16. Guo, Z.; Wittman, T.; Osher, S. L1 unmixing and its application to hyperspectral image enhancement. *Proc. SPIE* **2009**, *7334*, 579–587. [CrossRef]
17. Zhang, Y.; Fan, X.; Zhang, Y.; Wei, R. Linear spectral unmixing with generalized constraint for hyperspectral imagery. In Proceedings of the IEEE International Geoscience and Remote Sensing Symposium (IGARSS), Munich, Germany, 22–27 July 2012; pp. 4106–4109.
18. Agathos, A.; Li, J.; Bioucas-Dias, J.M.; Plaza, A. Robust minimum volume simplex analysis for hyperspectral unmixing. In Proceedings of the IEEE International Conference on Acoustics, Speech and Signal Processing (ICASSP), Florence, Italy, 4–9 May 2014; pp. 1582–1586.
19. Themelis, K.; Rontogiannis, A.; Koutroumbas, K. A soft-constrained MAP estimator for supervised hyperspectral signal unmixing. *IEEE Trans. Signal Process.* **2012**, *60*, 2799–2813. [CrossRef]
20. Jouni, M.; Mura, M.D.; Drumetz, L.; Comon, P. MultiHU-TD: Multifeature Hyperspectral Unmixing Based on Tensor Decomposition. *IEEE Trans. Geosci. Remote Sens.* **2023**, *61*, 5523621. [CrossRef]
21. Yao, J.; Hong, D.; Xu, L.; Meng, D.; Chanussot, J.; Xu, Z. Sparsity-Enhanced Convolutional Decomposition: A Novel Tensor-Based Paradigm for Blind Hyperspectral Unmixing. *IEEE Trans. Geosci. Remote Sens.* **2022**, *60*, 5505014. [CrossRef]
22. Qian, Y.; Xiong, F.; Zeng, S.; Zhou, J.; Tang, Y.Y. Matrix-Vector Nonnegative Tensor Factorization for Blind Unmixing of Hyperspectral Imagery. *IEEE Trans. Geosci. Remote Sens.* **2017**, *55*, 1776–1792. [CrossRef]
23. Bioucas-Dias, J. A variable splitting augmented Lagrangian approach to linear spectral unmixing. In Proceedings of the Workshop on Hyperspectral Image and Signal Processing: Evolution in Remote Sensing, Grenoble, France, 26–28 August 2009.
24. Li, Y.; Tan, T. An initially robust minimum simplex volume-based method for linear hyperspectral unmixing. *Int. J. Remote Sens.* **2024**, *45*, 1033–1058. [CrossRef]
25. Li, J.; Bioucas-Dias, J.M. Minimum Volume Simplex Analysis: A Fast Algorithm to Unmix Hyperspectral Data. In Proceedings of the IEEE International Geoscience and Remote Sensing Symposium, Boston, MA, USA, 7–11 July 2008; Volume 3, pp. 250–253. [CrossRef]

26. Li, Y.; Tan, T. A new convex model for linear hyperspectral unmixing. *J. Comput. Appl. Math.* **2024**, *441*, 115708. [CrossRef]
27. Heinz, D.; Chang, C.I. Fully constrained least squares linear spectral mixture analysis method for material quantification in hyperspectral imagery. *IEEE Trans. Geosci. Remote Sens.* **2001**, *39*, 529–545. [CrossRef]
28. Eckstein, J.; Bertsekas, D.P. On the Douglas—Rachford splitting method and the proximal point algorithm for maximal monotone operators. *Math. Program.* **1992**, *55*, 293–318. [CrossRef]
29. Zouaoui, A.; Muhawenayo, G.; Rasti, B.; Chanussot, J.; Mairal, J. Entropic Descent Archetypal Analysis for Blind Hyperspectral Unmixing. *IEEE Trans. Image Process.* **2023**, *32*, 15. [CrossRef] [PubMed]
30. Nascimento, J.M.P.; Dias, J.M.B. Vertex component analysis: A fast algorithm to unmix hyperspectral data. *IEEE Trans. Geosci. Remote Sens.* **2005**, *43*, 898–910. [CrossRef]
31. Tao, X.; Paoletti, M.E.; Wu, Z.; Haut, J.M.; Ren, P.; Plaza, A. An Abundance-Guided Attention Network for Hyperspectral Unmixing. *IEEE Trans. Geosci. Remote Sens.* **2024**, *62*, 5505414. [CrossRef]
32. Tao, X.; Koirala, B.; Plaza, A.; Scheunders, P. A New Dual-Feature Fusion Network for Enhanced Hyperspectral Unmixing. *IEEE Trans. Geosci. Remote Sens.* **2024**, *62*, 5540113. [CrossRef]
33. Chang, C.I.; Chen, S.Y.; Li, H.C.; Chen, H.M.; Wen, C.H. Comparative Study and Analysis Among ATGP, VCA, and SGA for Finding Endmembers in Hyperspectral Imagery. *IEEE J. Sel. Top. Appl. Earth Obs. Remote Sens.* **2016**, *9*, 4280–4306. [CrossRef]
34. Boyd, S.; Parikh, N.; Chu, E.; Peleato, B.; Eckstein, J. Distributed optimization and statistical learning via the alternating direction method of multipliers. *Found. Trends Mach. Learn.* **2011**, *3*, 1–122. [CrossRef]

Disclaimer/Publisher's Note: The statements, opinions and data contained in all publications are solely those of the individual author(s) and contributor(s) and not of MDPI and/or the editor(s). MDPI and/or the editor(s) disclaim responsibility for any injury to people or property resulting from any ideas, methods, instructions or products referred to in the content.